

# Supercurrents in Josephson junctions with chiral molecular potentials

Oleg Kuliashov,<sup>1</sup> Alberto Cappellaro,<sup>2,3,4</sup> Oded Millo,<sup>5</sup> Yossi Paltiel,<sup>1</sup> Mikhail Lemeshko,<sup>4</sup> and Ragheed Alhyder<sup>4,\*</sup>

<sup>1</sup>*Applied Physics Department, The Hebrew University of Jerusalem, Jerusalem, Israel*

<sup>2</sup>*Dipartimento di Fisica ed Astronomia "G. Galilei",*

*Università degli Studi di Padova, via Marzolo 8, 35131 Padova, Italy*

<sup>3</sup>*National Institute of Nuclear Physics (INFN), Padova Section, Via Marzolo 8, 35131 Padova, Italy*

<sup>4</sup>*Institute of Science and Technology Austria (ISTA), Am Campus 1, 3400 Klosterneuburg, Austria*

<sup>5</sup>*The Racah Institute of Physics, The Hebrew University of Jerusalem, 91904 Jerusalem, Israel*

The influence of chiral molecular potentials on phase-coherent transport in superconducting Josephson junctions is investigated. Within a Bogoliubov–de Gennes tight-binding framework, an SNS junction functionalized by adsorbed chiral molecules is modeled, where electrostatic gradients generated by the molecules induce spin–orbit coupling in the normal region. The equilibrium charge current–phase relation is found to remain largely insensitive to molecular chirality in symmetric, zero-field configurations. In contrast, the spin supercurrent exhibits a pronounced chirality-dependent response, with opposite enantiomers producing distinct and anisotropic spin-polarized Josephson currents. The resulting handedness contrast can be enhanced through control parameters such as molecular orientation and the strength of the induced spin–orbit coupling. The temperature dependence of these currents further shows that the chirality-dependent signatures persist across a range of temperatures well below the superconducting critical temperature. These results establish Josephson interferometry as a phase-sensitive and accessible platform for detecting molecular chirality and highlight spin-polarized superconducting transport as a promising route toward integrating chiral molecular functionality into superconducting spintronic devices.

## I. INTRODUCTION

Chirality is a geometric property of matter that has far reaching consequences across chemistry, biology, and condensed matter physics, because it distinguishes structures that are related by spatial inversion but cannot be continuously deformed into one another. In molecular settings, opposite enantiomers have the same energy but coexist with strikingly different functional behavior, which is why chirality is central to stereospecific chemistry and to the emergence of biological homochirality in living systems [1–3]. At the same time, the role chirality plays in the electronic and magnetic properties of materials is increasingly investigated, since it can imprint handedness onto transport and response functions once spin and orbital degrees of freedom are involved [4]. Exploiting these effects to establish scalable ways to interrogate chirality through robust physical observables remains an active challenge, complementing powerful spectroscopic approaches that access chirality through light matter interactions or enantiomer specific rotational responses [5].

A particularly influential development in this direction is chirality induced spin selectivity (CISS), where charge transport through chiral systems becomes correlated with spin polarization [6–11]. Experiments have connected such spin selectivity to functionality ranging from chiral molecular spin filters and enantiospecific interactions with magnetic substrates to magnetization control driven by adsorbed chiral layers [7–33]. Theoretical progress has clarified multiple microscopic routes that can generate sizable spin selectivity while also highlighting open

questions regarding quantitative modeling, the role of environment and dissipation, and the precise symmetry requirements for chirality specific signals in realistic devices [27, 34–39]. This combination of broad relevance and unresolved microscopic structure motivates the search for device platforms where chirality dependent physics can be amplified and read out reliably.

Josephson junctions provide a natural arena for such an approach because they convert subtle changes in quantum phase accumulation into macroscopic currents that can be measured with exquisite precision [40]. Their equilibrium supercurrent is carried by Andreev processes and bound states whose phase dispersion is controlled by scattering phases and spin dependent structure in their normal region [41–44]. In practice, Josephson devices form the backbone of superconducting electronics, serving both as ultrasensitive interferometers in SQUID based metrology and as engineered nonlinear elements in leading quantum information architectures [45–49]. The same phase coherence that enables these applications also makes Josephson junctions exceptionally responsive to spin orbit coupling and spin active scattering, including regimes where symmetry permits anomalous phase shifts or unconventional current components [50–53]. More broadly, recent experiments have demonstrated that structural chirality can strongly influence quantum transport phenomena, for example leading to nonreciprocal superconducting currents in Josephson junctions formed from opposite-handed crystals [54].

These observations motivate a synergy between CISS-based molecular physics and superconducting interferometry, in which a chiral molecular texture acts as a spatially structured spin orbit and potential landscape that reshapes Andreev transport. Experimental indica-

\* ragheed.alhyder@ista.ac.at

tions that chiral molecular layers can couple to superconducting states and induce magnetic related signatures strengthen this perspective and motivate superconducting circuits as a practical readout modality for molecular chirality [55]. In parallel, it was shown that chiral molecular potentials can generate symmetry controlled chirality dependent transport responses on magnetized surfaces, with a crucial dependence on molecular orientation and electrostatic gradients [38]. These results frame chiral molecular junction functionalization as a tunable route to spin active superconducting junctions whose response can be engineered without requiring microscopic state resolution.

Here, we develop a Bogoliubov de Gennes transport framework for SNS Josephson junctions functionalized by chiral molecular textures, and we show how chirality enters superconducting observables through spin dependent scattering phases accumulated in the normal region. We compute both the charge current phase relation and equilibrium spin supercurrents and demonstrate that chirality contrast is naturally enhanced by control knobs that activate interferometric sensitivity. These include orbital magnetic field patterns and the strength of molecule induced spin orbit coupling. We further analyze temperature dependence of these currents, which identifies the regime where chirality-dependent signatures persist despite thermal smearing. Taken together, these results position Josephson interferometry as an experimentally accessible route to chirality detection in electronic nanodevices, while simultaneously providing a controlled setting to investigate the interplay of chiral spin physics and superconducting phase coherence.

## II. MODEL

We model an SNS Josephson junction on a two-dimensional lattice with lattice constant  $a$ , with length  $L$  and width  $W$ . Two superconducting leads occupy the regions  $x < x_\ell$  (left lead) and  $x \geq x_r$  (right lead), while the normal component spans  $x_\ell \leq x < x_r$ . The phase bias between the superconductors is denoted by  $\phi$ .

We work in the Nambu spinor basis  $\hat{\Psi}_i = (\hat{c}_{i\uparrow}, \hat{c}_{i\downarrow}, \hat{c}_{i\uparrow}^\dagger, \hat{c}_{i\downarrow}^\dagger)^\top$ , and use Pauli matrices  $\boldsymbol{\tau} = (\tau_x, \tau_y, \tau_z)$  in particle-hole (Nambu) space and  $\boldsymbol{\sigma} = (\sigma_x, \sigma_y, \sigma_z)$  in spin space, with identities  $\tau_0$  and  $\sigma_0$ .

The mean-field Bogoliubov-de Gennes Hamiltonian is written as

$$\hat{H}_{\text{BdG}}(\phi) = \frac{1}{2} \sum_{ij} \hat{\Psi}_i^\dagger \begin{pmatrix} h_{ij} & \Delta_{ij}(\phi) \\ \Delta_{ij}^\dagger(\phi) & -h_{ij}^* \end{pmatrix} \hat{\Psi}_j, \quad (1)$$

where  $i, j$  label lattice sites and  $h_{ij}$  ( $\Delta_{ij}$ ) are  $2 \times 2$  matrices in spin space. The normal-state Hamiltonian  $h$  is decomposed as  $h = h_{\text{kin}} + h_Z$ , where  $h_{\text{kin}}$  is the kinetic energy including the chemical potential  $(h_{\text{kin}})_{ij} = (4t - \mu) \sigma_0 \delta_{ij} - t \sigma_0 \delta_{\langle ij \rangle}$ , with nearest-neighbor hopping  $t > 0$ , the onsite term  $4t$  is the standard shift that places

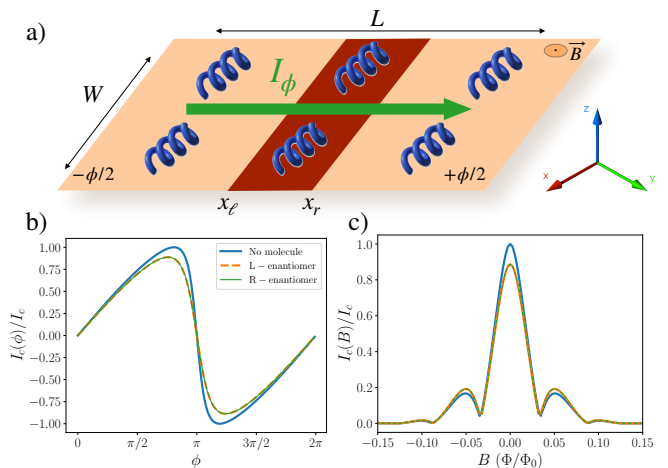


Figure 1. **(a)** Schematic of the Josephson junction considered throughout this work. Two superconducting leads with order-parameter phases  $\mp\phi/2$  are connected through a normal weak link (dark region) with adsorbed chiral molecular structures on top. The equilibrium supercurrent  $I_\phi$  flows along the transport direction in response to the gauge-invariant phase bias  $\phi$ . An out-of-plane magnetic field  $B\hat{z}$  threads flux through the junction area and produces interference of transverse supercurrent paths. **(b)** Current–phase relation at zero field,  $I_c(\phi) \equiv I(\phi, B=0)$ . While the molecular texture visibly renormalizes the overall Josephson response relative to the no-molecule reference, the two enantiomers yield overlapping charge supercurrents in this parameter set, consistent with chirality entering predominantly through spin-dependent structure of the Andreev states, robust chirality readout is therefore obtained from symmetry-breaking configurations such as magnetic-field interference and spin-sensitive transport observables studied in the following sections. **(c)** Fraunhofer response: critical current  $I_c(B) = \max_\phi |I(\phi, B)|$  normalized to its zero-field value, comparing the reference junction without molecules (blue) to junctions functionalized by left- and right-handed enantiomers (orange and green).

the band minimum at  $-\mu$ ,  $\delta_{\langle ij \rangle} = 1$  for nearest neighbors and 0 otherwise. A magnetic field along  $\hat{z}$  is included through a Zeeman term  $(h_Z)_{ij} = h_z \sigma_z \delta_{ij}$ .

Superconductivity is imposed through an onsite spin-singlet pairing potential in the lead regions with a phase difference  $\phi$  across the junction:

$$\Delta_{ij}(\phi) = \Delta_i e^{i\phi_i} (i\sigma_y) \delta_{ij}, \quad (2)$$

with the piecewise-constant phase profile  $\phi_i = -\phi/2$  for  $x_i < x_\ell$ ,  $\phi_i = 0$  for  $x_\ell \leq x_i < x_r$ , and  $\phi_i = +\phi/2$  for  $x_i \geq x_r$ . Orbital effects are included through a Peierls phase on nearest-neighbor hoppings. Using a Landau-gauge in which only hoppings along  $\hat{y}$  acquire a phase, and only within the normal region  $x_\ell \leq x < x_r$ , we write the hopping term  $-t e^{i\theta_{ij}\tau_z}$ , with  $\theta_{ij} = B \kappa x_j (y_i - y_j)$ , The explicit  $\tau_z$  again ensures opposite coupling for particles and holes. When orbital effects are not required one sets  $B = 0$ .

The molecule contributes a scalar onsite term to the

BdG Hamiltonian,

$$\hat{H}_{\text{mol}}^{(0)} = \sum_i \hat{\Psi}_i^\dagger \left[ V_{\text{mol}}(\mathbf{r}_i) \tau_z \otimes \sigma_0 \right] \hat{\Psi}_i, \quad (3)$$

where  $V_{\text{mol}}(\mathbf{r})$  is the electrostatic potential generated by the molecule, evaluated at lattice positions  $\mathbf{r}_i = (x_i, y_i)$ . The explicit  $\tau_z$  structure ensures that electrons and holes experience opposite scattering potentials. We model each adsorbed molecule by an electrostatic potential [35, 38]

$$V_{\text{mol}}(\mathbf{r}) = \mathcal{E} \cdot \mathbf{r}' \exp \left[ -\frac{1}{2} \left( \frac{x'^2}{\ell_x^2} + \frac{y'^2}{\ell_y^2} + \frac{z'^2}{\ell_z^2} \right) \right], \quad (4)$$

where  $\mathbf{r}' = (x', y', z')$  are coordinates in the molecular frame, obtained by rotating the molecule about the  $x$  axis by an angle  $\theta$ , i.e.  $\mathbf{r}' = R_x(\theta)(\mathbf{r} - \mathbf{r}_m)$  with  $R_x(\theta)$  the standard right-handed rotation matrix, and  $\mathbf{r}_m = (x_m, y_m, 0)$  the molecular center. The parameters  $\ell_{x,y,z}$  set the anisotropic spatial extent of the potential. The linear prefactor is controlled by an effective internal field  $\mathcal{E} = (\mathcal{E}_x, \mathcal{E}_y, \mathcal{E}_z)$ , which we parameterize in terms of an effective molecular dipole moment  $\boldsymbol{\mu} = (\mu_x, \mu_y, \mu_z)$  as  $\mathcal{E}_\nu = 8e\mu_\nu/\ell_\nu^3$ , with  $\nu \in \{x, y, z\}$ , and  $e$  the electron charge in our dimensionless convention. The explicit molecular parameters used in the simulations are summarized in Appendix A.

In the present model, opposite molecular chiralities are implemented by a single discrete parameter  $\chi = \pm 1$  multiplying the  $y$ -component of the molecular moment  $\mu_y$ , while all other parameters are held fixed. This choice corresponds to a mirror operation with respect to the  $xz$  plane in the molecular parameterization (i.e.,  $y \mapsto -y$  in the molecular frame), which reverses the handedness of the potential. Independently, the continuous angle  $\theta$  controls the molecular orientation relative to the junction plane. The rotation ensures the mirror symmetry breaking required for chirality-induced effects, as taking the mirror symmetric counterpart of the molecule when  $\theta \neq 0$  is equivalent to applying a mirror symmetry transformation to the entire junction around the  $xz$  plane.

Spin-orbit effects arise from the inhomogeneous molecular potential via a Pauli (Rashba-like) coupling [50], implemented on the lattice as spin-dependent nearest-neighbor hoppings

$$\hat{H}_{\text{mol}}^{(\text{SO})} = \sum_{\langle ij \rangle} \hat{\Psi}_i^\dagger \left[ -i\alpha_{\text{SO}} (\mathcal{E}(\mathbf{r}_i) \times \hat{\mathbf{d}}_{ij}) \cdot (\tau_z \otimes \boldsymbol{\sigma}) \right] \hat{\Psi}_j + \text{H.c.}, \quad (5)$$

where  $\alpha_{\text{SO}}$  is the spin-orbit parameter indicating the strength of the coupling,  $\mathcal{E}(\mathbf{r}) \equiv -\nabla V_{\text{mol}}(\mathbf{r})$  is the local effective electric field,  $\hat{\mathbf{d}}_{ij} = (\mathbf{r}_i - \mathbf{r}_j)/|\mathbf{r}_i - \mathbf{r}_j|$  for nearest neighbors, and  $\tau_z$  enforces the opposite sign in the hole sector.

We work in dimensionless tight-binding units, setting the lattice spacing and nearest-neighbor hopping to unity ( $a \equiv 1, t \equiv 1$ ). All energies in the Hamiltonian are therefore measured in units of  $t$ , and temperature is measured in units of  $t/k_B$  (equivalently  $k_B \equiv 1$ ). Orbital magnetic

effects enter through a Peierls phase on hoppings with the dimensionless choice  $\theta_{ij} = Bx_j(y_i - y_j)$  (i.e. Peierls prefactor set to unity). Physical units can be restored by reinstating  $\hbar$  and  $|e|$  in  $\theta_{ij} = (|e|/\hbar) \int_{\mathbf{r}_j}^{\mathbf{r}_i} \mathbf{A} \cdot d\boldsymbol{\ell}$  and identifying  $t = \hbar^2/(2m^*a^2)$ , so that all dimensionless energies map to physical scales by multiplication with  $t$ .

### III. RESULTS

We perform numerical simulations on the Hamiltonian described previously by exact diagonalization of the BdG Hamiltonian in Eq. (1) for a given set of parameters, which yields the quasiparticle spectrum  $\{E_n(\phi, B)\}$  and eigenstates  $\{|n\rangle\}$  as a function of superconducting phase bias  $\phi$  and orbital magnetic field  $B$ . We then compute the equilibrium charge and spin supercurrents from these spectral data with the help of the Kwant package [56, 57] as detailed below. The resulting currents are analyzed as a function of control parameters such as the effective SOC strength  $\alpha$ , molecular orientation  $\theta$ , and temperature  $T$ .

#### A. Junction geometry and computational protocol

Figure 1(a) summarizes the superconducting-normal-superconducting (SNS) junction geometry studied in this work. Two superconductors with order-parameter phases  $\mp\phi/2$  are coupled through a normal link, with chiral molecular texture adsorbed on the surface of the junction. The handedness of this texture is encoded by a chirality index  $\chi = \pm 1$  (corresponding to left- and right-handed enantiomers), and it generates a spin-dependent region through an effective spin-orbit coupling tied to the electrostatic gradients produced by the molecule. An external magnetic field  $B\hat{\mathbf{z}}$  can generate flux through the junction area, enabling interference of transverse supercurrent trajectories and thereby providing an experimentally direct probe of phase-coherent transport.

For a given set of microscopic parameters, we compute the equilibrium Josephson current from the BdG quasiparticle spectrum  $\{E_n(\phi, B)\}$  via the standard thermodynamic expression

$$I(\phi, B) = \frac{2e}{\hbar} \sum_{n>0} \tanh\left(\frac{E_n(\phi, B)}{2T}\right) \frac{\partial E_n(\phi, B)}{\partial \phi}, \quad (6)$$

where the sum runs over positive BdG energies. This formulation makes explicit how molecule-induced spin-active scattering reshapes the phase sensitivity of the spectrum and hence the supercurrent response.

Figure 1(b) displays the equilibrium current-phase relation at  $B = 0$  for three configurations: a reference junction without molecules and junctions functionalized by left- and right-handed enantiomers. In the absence of molecules, the current exhibits the characteristic periodic behavior of an SNS junction. Introducing the molecular texture renormalizes the Josephson response, modi-

fyng the overall critical current and slightly reshaping the current–phase relation, reflecting the fact that the molecule modifies the effective transparency and the spin-dependent phase accumulation of Andreev quasiparticles. The phase dispersion of the low-energy Andreev bound states underlying the Josephson response is illustrated in Appendix D.

In addition, we show in figure 1(c) the Fraunhofer response, i.e., the orbital-field dependence of the critical current  $I_c(B) = \max_\phi |I(\phi, B)|$ , normalized to its zero-field value. The out-of-plane field  $B\hat{z}$  induces a position-dependent gauge-invariant phase accumulation across the junction width, leading to interference between supercurrent contributions carried by different transverse trajectories. The resulting  $I_c(B)$  exhibits the familiar lobe structure characteristic of Josephson interferometry, providing a sensitive and experimentally standard diagnostic of phase-coherent transport through the weak link. Relative to the no-molecule reference, the molecular texture again produces a systematic suppression and reshaping of the envelope.

A notable feature in both figures is that the charge current for the two enantiomers is nearly indistinguishable in this parameter set. This behavior is consistent with chirality entering predominantly through the spin-dependent structure of the quasiparticle states in the normal region, while the charge supercurrent at zero field remains largely constrained by equilibrium symmetries. In particular, in the absence of an explicit time-reversal-breaking perturbation, opposite enantiomers yield similar energies and therefore similar charge currents. This motivates complementing charge-transport interferometry with probes that couple more directly to the spin sector (e.g., spin-polarized Josephson observables) and, crucially, exploring regimes with enhanced spin mixing and explicit time-reversal breaking, where enantiomer-dependent corrections to transport become parametrically larger.

## B. Spin-polarized Josephson transport and tuning by spin–orbit coupling

Figure 2 summarizes how the charge and spin supercurrents evolve as the effective spin–orbit coupling strength  $\alpha$  associated with the molecular electrostatic gradients is tuned. The charge current is evaluated from Eq. (6). The spin-current components are computed from the equilibrium expectation value of the corresponding current operators across a cut through the junction: denoting by  $\hat{J}^a$  the spin-current operator for spin polarization  $a \in \{x, y, z\}$ , we evaluate

$$I_s^\nu = \frac{1}{2} \sum_{n>0} \tanh\left(\frac{E_n}{2T}\right) \langle n | \hat{J}^\nu | n \rangle, \quad (7)$$

where  $|n\rangle$  are BdG eigenstates with positive energies and the prefactor avoids double counting associated with the

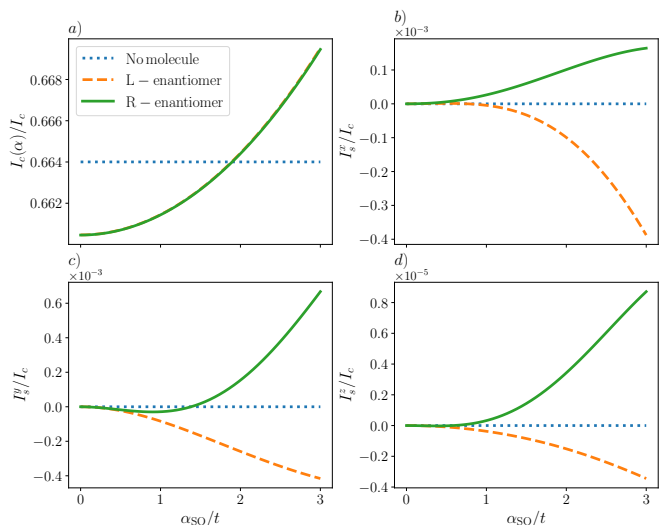


Figure 2. Dependence of charge and spin currents on the effective spin–orbit coupling strength  $\alpha_{\text{SO}}$ . (a) The normalized charge critical current varies only weakly with handedness, indicating that the primary molecular effect in the charge sector is a renormalization of the junction transparency. (b–d) In contrast, finite spin currents emerge in the presence of the molecular potential and grow with increasing  $\alpha_{\text{SO}}$ , with opposite enantiomers producing spin currents of opposite sign. Parameters:  $W = 8$ ,  $L = 26$ ,  $\mu = 0.5$ ,  $\Delta_0 = 0.2$ ,  $h_z = 0$ ,  $\theta = \pi/4$ , and  $B = 0$ .

Nambu representation. A derivation of this expression within the Bogoliubov–de Gennes formalism is outlined in Appendix B.

Two robust trends are apparent in Fig. 2. First, the charge response shows only a weak dependence on chirality for the parameters considered: while introducing the molecular texture produces a clear, systematic renormalization of the charge critical current relative to the no-molecule reference as  $\alpha$  is increased, the left- and right-handed enantiomers remain nearly indistinguishable on the scale of panel (a). This indicates that, here, the leading charge-current effect of the molecules is largely scattering represented in an overall change in effective transparency and phase dispersion. Second, the spin supercurrents provide a much more direct readout of molecular handedness, reflecting the spin-dependent phase accumulated by quasiparticles while propagating through the chiral molecular potential, which depends on the molecular orientation angle  $\theta$ . In the no-molecule reference, all spin-current components remain strongly suppressed across the full  $\alpha$  range, consistent with the absence of spin-active scattering. Once the molecular field is present, finite spin currents develop and grow monotonically with the effective SOC strength  $\alpha_{\text{SO}}$ . In the superconducting regime these currents acquire a phase-coherent Josephson component originating from the spin structure of the Andreev states, and the two enantiomers separate clearly in each spin channel (Fig. 2 (b)–(d)).

The chirality dependence is also strongly anisotropic

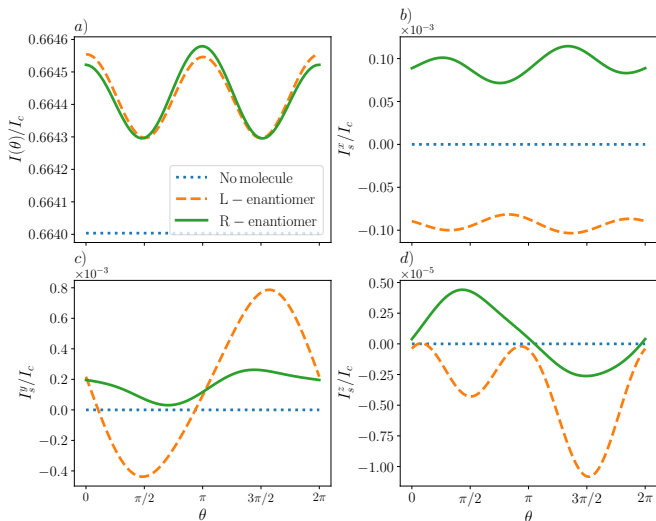


Figure 3. Angular dependence of the charge and spin currents on the molecular tilt angle  $\theta$ . Rotating the molecular electrostatic texture modifies the effective spin-orbit field experienced by quasiparticles in the junction. While the charge current remains only weakly sensitive to chirality, the spin-current components show a pronounced orientation dependence and opposite responses for the two enantiomers. Parameters:  $W = 8$ ,  $L = 26$ ,  $\mu/t = 0.5$ ,  $\Delta_0/t = 0.2$ ,  $\alpha_{\text{SO}}/t = 2$ ,  $h_z = 0$ , and  $B = 0$ .

where the magnitudes and  $\alpha$ -scalings differ between  $I_s^x$ ,  $I_s^y$ , and  $I_s^z$ , reflecting the spatial inhomogeneity and anisotropy of the molecular electrostatic landscape, so the effective SOC field and the resulting phase accumulation along Andreev trajectories are not equivalent for the three spin projections. Overall, Fig. 2 identifies  $\alpha$  as a practical control knob for amplifying spin-polarized Josephson signatures of chirality. This motivates using spin-resolved observables (and, where appropriate, additional symmetry-breaking fields) as the primary experimental pathway to robust handedness detection in superconducting weak links.

### C. Angular dependence and symmetry constraints

In fig. 3, we show how the Josephson response varies with the molecular tilt angle  $\theta$ , which rotates the molecular electrostatic texture relative to the junction plane and thereby changes the structure of the effective spin-orbit field seen by traversing quasiparticles [33]. The curves are obtained by repeating the equilibrium calculations described above while varying  $\theta$  at fixed superconducting phase bias and fixed  $\alpha$ . Formally,  $\theta$  modifies the spatial gradients of the scalar potential  $V(\mathbf{r})$  and hence the effective spin-orbit term of the generic form  $(\nabla V \times \mathbf{p}) \cdot \boldsymbol{\sigma}$ , which in turn alters the spin structure of the Andreev eigenstates entering Eqs. (6) and (7).

The effect of chirality is more accentuated in fig. 3 where chirality detection can be optimized by orienta-

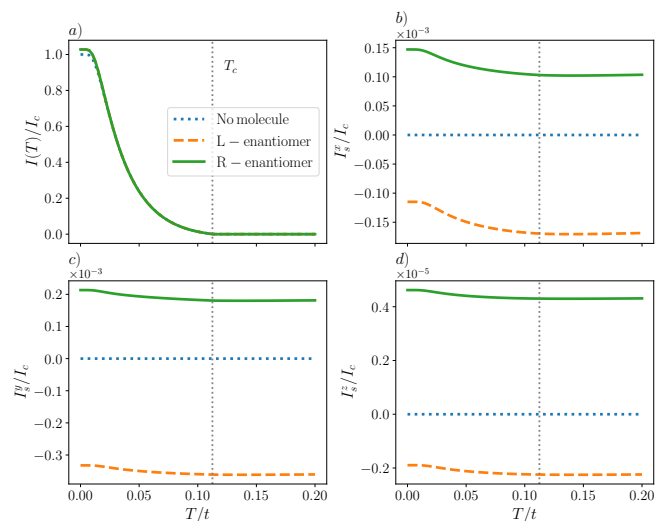


Figure 4. Temperature dependence of charge and spin currents in the chiral-molecule Josephson junction. (a) The normalized charge current decreases with increasing temperature and vanishes as the superconducting gap closes near  $T_c$ . (b–d) The spin-current components are progressively modified with temperature but retain a residual offset above  $T_c$ . This offset reflects an equilibrium spin-current background generated by the spin-orbit-coupled molecular potential rather than a phase-coherent Josephson contribution. Parameters:  $W = 8$ ,  $L = 26$ ,  $\mu/t = 0.5$ ,  $\Delta_0/t = 0.2$ ,  $\alpha_{\text{SO}}/t = 2$ ,  $\theta = \pi/4$ , and  $B = 0$ .

tional control. For small tilts, the induced spin-orbit field has a dominant component set by the in-plane gradients, and the resulting spin supercurrents follow a characteristic angular trend reflecting the junction symmetries. As  $\theta$  is increased, different gradient components contribute, leading to a redistribution among spin-current components and, correspondingly, to a modified charge current. The comparison between  $\chi = \pm 1$  shows that the chirality-odd response persists across a broad angular range, while specific angles can maximize the contrast between enantiomers. This angular tunability is particularly relevant experimentally because it suggests that geometric alignment (or controlled adsorption orientation) can be used to amplify chirality-sensitive observables without changing material parameters.

### D. Temperature dependence and experimental feasibility

In Fig. 4 we test the robustness of the chiral signatures against thermal effects. Temperature enters the equilibrium currents in two complementary ways. First, it controls quasiparticle occupations through the factors  $\tanh(E_n/2T)$  in Eqs. (6) and (7), progressively reducing the contribution of higher-energy states and smoothing the phase sensitivity of the spectrum. Second, it suppresses the superconducting order parameter in the leads,

which directly reduces the Andreev level dispersion and hence the spectral slopes that control both charge and spin supercurrents. We incorporate this second effect by taking the lead gap  $\Delta(T)$  from the BCS temperature dependence.

The resulting trends in Fig. 4 are consistent with this physical picture. The charge Josephson response decreases monotonically with  $T$  and is strongly suppressed as the gap  $\Delta(T)$  closes and the presence of the chiral molecule decreases the current. In contrast, the spin-current components exhibit two distinct contributions. The dominant phase-coherent component decreases with increasing temperature in parallel with the suppression of the superconducting proximity effect. However, a residual signal remains even when  $T \gtrsim T_c$ . This offset originates from the spin-orbit-coupled molecular texture and reflects an equilibrium spin-current background of the normal-state Hamiltonian rather than a Josephson contribution. A decomposition of the spin current into normal-state and superconducting contributions is presented in Appendix C. Such equilibrium spin currents are known to arise in systems with broken inversion symmetry and spin-orbit coupling when the conventional spin-current operator is used [58, 59]. Therefore, the superconductivity-enabled contribution can be identified operationally as the component that scales with the superconducting gap  $\Delta(T)$ .

#### IV. CONCLUSION

We have shown that chiral molecular electrostatic textures, when integrated into an SNS Josephson junction, act as a tunable source of spin-dependent scattering that restructures the Andreev bound-state spectrum and thereby modifies equilibrium supercurrents. Across the explored parameter space, the most robust chirality-sensitive signatures arise in *spin-polarized* Josephson transport: opposite enantiomers generate systematically different spin supercurrents, with a pronounced anisotropy among spin components that reflects the non-trivial spatial structure of the molecular potential and its associated SOC field. By contrast, the equilibrium charge current remains nearly identical in symmetric, zero-field configurations, consistent with chirality entering primarily through the spin texture of quasiparticle states while the total charge response is constrained by equilibrium symmetries. Importantly, the spin response is not only chirality-dependent but also tunable, where varying the effective SOC strength and molecular orientation provides practical control knobs that amplify the handedness contrast without requiring changes to the junction geometry. Our results complement recent efforts to engineer quantum transport phenomena through symmetry control in condensed matter systems, including recent demonstrations of nonreciprocal superconducting transport in structurally chiral Josephson junctions [54].

From an application standpoint, these results motivate

a phase-sensitive strategy for chiral sensing using superconducting circuits. Chirality can in general be detected through spin-selective transport processes. However, the Josephson platform probes the phase accumulated by quasiparticles traversing the chiral molecular potential. The resulting interferometric response therefore provides direct access to the coherence of the underlying spin-dependent scattering processes. Rather than relying on microscopic spectroscopy, chirality can thus be inferred from phase-sensitive transport observables such as differential Fraunhofer patterns and spin-polarized Josephson currents.

#### ACKNOWLEDGMENTS

Oleg Kuliashov is funded by the European Union, in the framework of the Marie Skłodowska-Curie Actions-CISSE Doctoral Network, under Grant Agreement no. 101071886. Views and opinions expressed are however, those of the author(s) only and do not necessarily reflect those of the European Union or the European Research Executive Agency (REA). Neither the European Union nor the granting authority can be held responsible for them. R. A. received funding from the Austrian Academy of Science ÖAW grant No. PR1029OEAW03.

#### Appendix A: Molecular potential and simulation parameters

In the numerical simulations presented in this work the chiral molecule is modeled through an electrostatic potential acting on the lattice sites of the normal region. The functional form of this potential follows the parametrization introduced in Refs. [35, 38] and reproduced here for completeness.

The molecular electrostatic potential is written as

$$V_{\text{mol}}(\mathbf{r}) = E \cdot \mathbf{r}' \exp \left[ -\frac{1}{2} \left( \frac{x'^2}{\ell_x^2} + \frac{y'^2}{\ell_y^2} + \frac{z'^2}{\ell_z^2} \right) \right], \quad (\text{A1})$$

where  $\mathbf{r}' = (x', y', z')$  denotes coordinates in the molecular frame. These coordinates are obtained from the laboratory frame position  $\mathbf{r} = (x, y, z)$  through a rotation around the  $x$  axis by an angle  $\theta$ ,  $\mathbf{r}' = R_x(\theta) (\mathbf{r} - \mathbf{r}_m)$ , with  $\mathbf{r}_m = (x_m, y_m, 0)$  the molecular center and  $R_x(\theta)$  the standard rotation matrix.

The parameters  $\ell_x$ ,  $\ell_y$ , and  $\ell_z$  control the spatial extent of the potential along the three molecular axes. The linear prefactor is determined by an effective internal electric field  $\mathcal{E} = (\mathcal{E}_x, \mathcal{E}_y, \mathcal{E}_z)$  related to a molecular dipole moment  $\boldsymbol{\mu}$  through  $\mathcal{E}_\nu = \frac{8e\mu_\nu}{\ell_\nu^3}$ , with  $\nu \in \{x, y, z\}$ . The Nambu basis ensures electrons and holes experience opposite scattering potentials.

Opposite molecular enantiomers are implemented by reversing the  $y$  component of the molecular dipole moment,  $\mu_y \rightarrow \chi \mu_y$ , with  $\chi = \pm 1$ ,

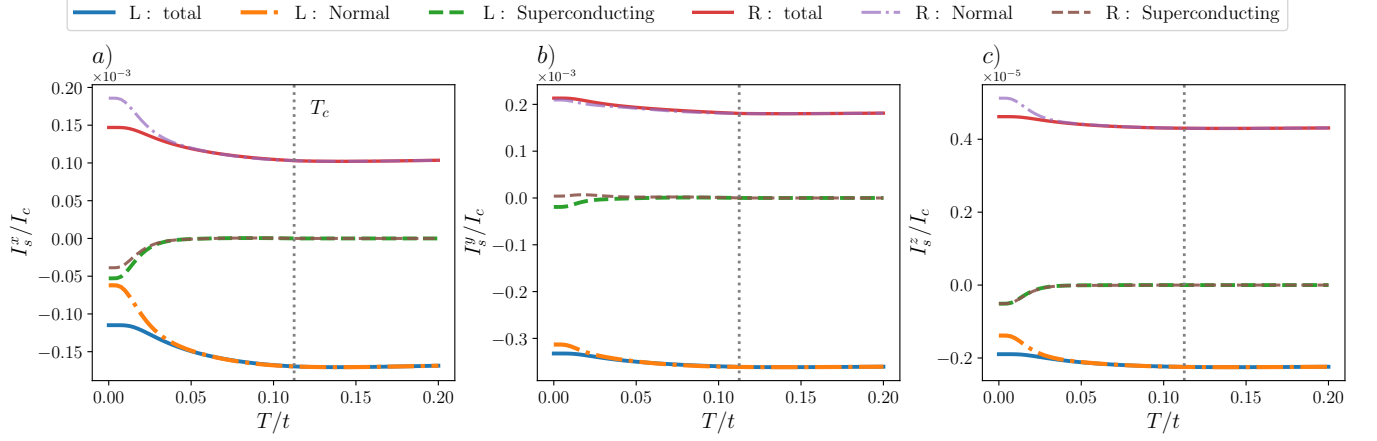


Figure A1. Decomposition of the spin current into normal-state and superconducting contributions. The total spin current  $I_s^a$  (solid lines) is separated into a normal-state background  $I_s^a(\Delta = 0)$  (dotted lines) and a superconducting component  $I_{s,SC}^a = I_s^a - I_s^a(\Delta = 0)$  (dash-dotted lines) for the left- and right-handed molecular enantiomers.

while all other parameters are kept fixed. This transformation corresponds to a mirror operation with respect to the  $xz$  plane in the molecular frame and reverses the handedness of the electrostatic texture.

Unless stated otherwise, all numerical results in this work use the same molecular parameters:  $\ell_x = 2.0$ ,  $\ell_y = 4.0$ ,  $\ell_z = 10.0$ , and dipole moments  $\mu_x = 2.4$ ,  $\mu_y = 5.0\chi$ ,  $\mu_z = 1.8$ . The molecular orientation angle is fixed to  $\theta = \pi/4$ , unless explicitly varied in the angular dependence calculations. We also use a factor of 0.01 to multiply the potential  $V_{\text{mol}}$  when it is included in the Hamiltonian, which ensures that the resulting spin-orbit coupling is not overcome by the kinetic energy and that the molecular potential acts as a perturbation rather than a dominant energy scale.

The molecule is positioned at the center of the junction, and the strength of the induced spin-orbit coupling is controlled by the dimensionless parameter  $\alpha_{\text{SO}}$  which can be varied.

## Appendix B: Current operators and numerical evaluation

The form of Eq. 7 follows directly from the thermal expectation value of a one-body operator in the Bogoliubov-de Gennes basis. Let  $\hat{J}^a$  denote the many-body operator associated with the spin-current matrix  $\hat{J}^a$ , with  $a \in \{x, y, z\}$  the spin polarization direction. In a lattice formulation the current is naturally defined on bonds between neighboring sites. Starting from the spin density operator  $s_i^a = \frac{1}{2}\Psi_i^\dagger(\tau_0 \otimes \sigma_a)\Psi_i$ , the corresponding spin-current operator follows from the continuity equation for spin density and can be written for a bond  $(i, j)$

as

$$\hat{J}_{ij}^a = \frac{i}{2} \left( \Psi_i^\dagger (\tau_0 \otimes \sigma_a) H_{ij} \Psi_j - \Psi_j^\dagger H_{ji} (\tau_0 \otimes \sigma_a) \Psi_i \right), \quad (\text{B1})$$

where  $H_{ij}$  denotes the Bogoliubov-de Gennes Hamiltonian matrix element connecting sites  $i$  and  $j$  (including both kinetic and spin-orbit hopping terms). The total spin current across a transverse cut of the junction is obtained by summing  $\hat{J}_{ij}^a$  over all bonds crossing that cut. In practice, after diagonalization of  $\hat{H}_{\text{BdG}}$ , the quasiparticle spectrum appears in particle-hole-symmetric pairs  $\pm E_n$ , with  $E_n > 0$ , and the equilibrium occupation of a quasiparticle mode is given by the Fermi function  $f(E_n) = 1/(e^{E_n/T} + 1)$ , where we use  $k_B \equiv 1$  throughout. In the BdG formalism, the expectation value of any bilinear operator can be written as a sum over the contributions of the  $\pm E_n$  partners. For the spin-current operator this gives

$$I_s^a = \frac{1}{2} \sum_{n>0} \left[ f(E_n) \langle n | \hat{J}^a | n \rangle + (1 - f(E_n)) \langle \bar{n} | \hat{J}^a | \bar{n} \rangle \right], \quad (\text{B2})$$

where  $|\bar{n}\rangle$  is the particle-hole partner of  $|n\rangle$  with energy  $-E_n$ . The prefactor 1/2 removes the double counting inherent to the Nambu representation.

Using particle-hole symmetry, the matrix elements of the current operator for the two partner states are related by  $\langle \bar{n} | \hat{J}^a | \bar{n} \rangle = -\langle n | \hat{J}^a | n \rangle$ , so that the two terms combine into

$$I_s^a = \frac{1}{2} \sum_{n>0} [1 - 2f(E_n)] \langle n | \hat{J}^a | n \rangle.$$

Using the identity  $1 - 2f(E) = \tanh\left(\frac{E}{2T}\right)$ , one obtains Eq. Eq. 7,

$$I_s^a = \frac{1}{2} \sum_{n>0} \tanh\left(\frac{E_n}{2T}\right) \langle n | \hat{J}^a | n \rangle. \quad (\text{B3})$$

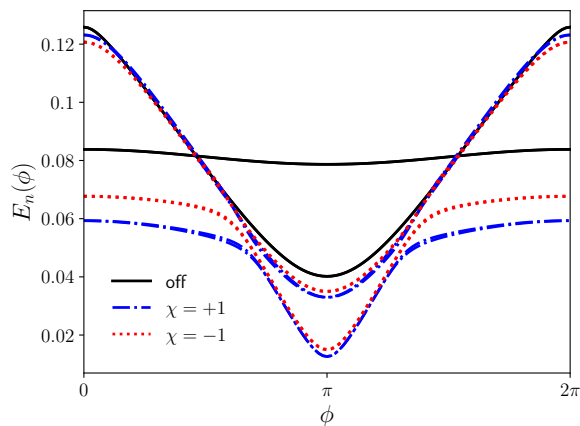


Figure A2. Low-energy Andreev bound-state branches  $E_n(\phi)$  obtained from diagonalization of the Bogoliubov–de Gennes Hamiltonian. Solid lines correspond to the junction without molecules, while dashed and dotted lines show the spectra for molecular potentials with opposite chiralities  $\chi = \pm 1$ .

This representation is convenient because the sum can be restricted to positive BdG energies only, while the thermal weight  $\tanh(E_n/2T)$  compactly accounts for the occupations of both members of each particle–hole pair. Equivalently, one may write the thermal factor as  $1 - 2f(E_n)$ , but the  $\tanh(E_n/2T)$  form is more compact and is standard in BdG expressions for equilibrium observables.

### Appendix C: Decomposition of the spin current

To clarify the physical origin of the spin currents shown in Fig. 4 of the main text, we decompose the total spin current into a normal-state contribution and a superconductivity-induced component. This separation is obtained by evaluating the spin current both in the superconducting junction and in the corresponding normal-state system where the pairing potential is set to zero. The superconducting contribution is then defined as

$$I_{s,SC}^a(T) = I_s^a(T) - I_s^a(T, \Delta = 0), \quad a \in \{x, y, z\}, \quad (\text{C1})$$

where  $I_s^a(T)$  is the equilibrium spin current of the superconducting junction and  $I_s^a(T, \Delta = 0)$  is the current obtained in the same structure in the absence of superconductivity.

Figure A1 shows this decomposition for the two molecular enantiomers. The normal currents arise from the

spin–orbit interaction generated by the chiral molecular potential. This contribution is essentially temperature independent and persists above the superconducting critical temperature [58, 59].

The superconducting contribution originates from the modification of the quasiparticle spectrum by superconductivity and therefore vanishes when the superconducting gap closes at  $T_c$ . As expected, this component is largest at low temperature and progressively decreases as  $T$  approaches  $T_c$ , reflecting the suppression of the superconducting gap and of the associated Andreev spectrum dispersion. The total spin current therefore results from the superposition of a chirality-dependent superconducting component and a normal-state spin current induced by the chiral spin–orbit interaction.

### Appendix D: Andreev bound-state spectrum and phase dispersion

To illustrate the spectral origin of the equilibrium Josephson response, we compute the low-energy positive Bogoliubov–de Gennes eigenvalues as a function of the superconducting phase difference  $\phi$ . For each value of  $\phi$ , the finite-system BdG Hamiltonian is diagonalized numerically and the eigenvalues closest to zero energy are extracted. The corresponding branches are then tracked between neighboring phase points by maximizing the overlap between eigenvectors, which yields a continuous representation of the low-energy phase-dependent spectrum.

Figure A2 shows the resulting low-energy branches for the junction without molecules and for junctions with the molecular potential present. These branches form the subgap sector responsible for the phase-sensitive Josephson response. In particular, the charge current is governed by the phase derivatives of the BdG energies (See Eq. (6)), so that changes in the spectral dispersion directly translate into changes in the current–phase relation. At low temperature, these low-energy Andreev branches dominate the Josephson current.

The comparison shows that the molecular potential modifies the low-energy phase dispersion relative to the reference junction without molecules, consistent with the molecule acting as a spin-dependent scatterer in the normal region. At the same time, the spectra for opposite enantiomers remain rather similar in this symmetric zero-field configuration, in agreement with the weak chirality dependence of the equilibrium charge current discussed in the main text.

[1] L. D. Barron, *Chemical Physics Letters* **123**, 423 (1986).  
 [2] Y. Saito and H. Hyuga, *Rev. Mod. Phys.* **85**, 603 (2013).  
 [3] D. G. Blackmond, *Cold Spring Harb. Perspect. Biol.* [10.1101/cshperspect.a032540](https://doi.org/10.1101/cshperspect.a032540) (2019).

[4] C. D. Aiello, J. M. Abendroth, M. Abbas, A. Afanasev, S. Agarwal, A. S. Banerjee, D. N. Beratan, J. N. Belling, B. Berche, A. Botana, J. R. Caram, G. L. Celardo, G. Cumiberti, A. Garcia-Etxarri, A. Dianat,

- I. Diez-Perez, Y. Guo, R. Gutierrez, C. Herrmann, J. Hithath, S. Kale, P. Kurian, Y.-C. Lai, T. Liu, A. Lopez, E. Medina, V. Mujica, R. Naaman, M. Noormandipour, J. L. Palma, Y. Paltiel, W. Petuskey, J. C. Ribeiro-Silva, J. J. Saenz, E. J. G. Santos, M. Solyanik-Gorgone, V. J. Sorger, D. M. Stemer, J. M. Ugalde, A. Valdes-Curiel, S. Varela, D. H. Waldeck, M. R. Wasielewski, P. S. Weiss, H. Zacharias, and Q. H. Wang, *ACS Nano* **16**, 4989 (2022).
- [5] D. Patterson, M. Schnell, and J. M. Doyle, *Nature* **497**, 475–477 (2013).
- [6] K. Ray, S. P. Ananthavel, D. H. Waldeck, and R. Naaman, *Science* **283**, 814 (1999).
- [7] Z. Xie, T. Z. Markus, S. R. Cohen, Z. Vager, R. Gutierrez, and R. Naaman, *Nano Letters* **11**, 4652 (2011).
- [8] R. Gutierrez, E. Díaz, R. Naaman, and G. Cuniberti, *Phys. Rev. B* **85**, 081404 (2012).
- [9] R. Naaman and D. H. Waldeck, *Annual Review of Physical Chemistry* **66**, 263 (2015).
- [10] R. Naaman, Y. Paltiel, and D. Waldeck, *Nature Reviews Chemistry* **3**, 1 (2019).
- [11] R. Naaman, Y. Paltiel, and D. H. Waldeck, *Accounts of Chemical Research* **53**, 2659 (2020).
- [12] K. Banerjee-Ghosh, O. B. Dor, F. Tassinari, E. Capua, S. Yochelis, A. Capua, S.-H. Yang, S. S. P. Parkin, S. Sarkar, L. Kronik, L. T. Baczewski, R. Naaman, and Y. Paltiel, *Science* **360**, 1331 (2018).
- [13] O. B. Dor, S. Yochelis, A. Radko, K. Vankayala, E. Capua, A. Capua, S.-H. Yang, L. T. Baczewski, S. S. P. Parkin, R. Naaman, and Y. Paltiel, *Nature Communications* **8**, 10.1038/ncomms14567 (2017).
- [14] A.-M. Guo and Q.-f. Sun, *Phys. Rev. Lett.* **108**, 218102 (2012).
- [15] A.-M. Guo and Q.-f. Sun, *Phys. Rev. B* **86**, 115441 (2012).
- [16] S. Varela, V. Mujica, and E. Medina, *Phys. Rev. B* **93**, 155436 (2016).
- [17] A. C. Aragonès, E. Medina, M. Ferrer-Huerta, N. Gimeno, M. Teixidó, J. L. Palma, N. Tao, J. M. Ugalde, E. Giral, I. Díez-Pérez, and V. Mujica, *Small* **13**, 1602519 (2017).
- [18] K. M. Alam and S. Pramanik, *Nanoscale* **9**, 5155 (2017).
- [19] H. Lu, J. Wang, C. Xiao, X. Pan, X. Chen, R. Brunecky, J. J. Berry, K. Zhu, M. C. Beard, and Z. V. Vardeny, *Science Advances* **5**, eaay0571 (2019).
- [20] M. Atzori and R. Sessoli, *Journal of the American Chemical Society* **141**, 11339 (2019).
- [21] M. Geyer, R. Gutierrez, V. Mujica, and G. Cuniberti, *The Journal of Physical Chemistry C* **123**, 27230 (2019).
- [22] X. Yang, C. H. van der Wal, and B. J. van Wees, *Phys. Rev. B* **99**, 024418 (2019).
- [23] A. Ghazaryan, M. Lemesko, and A. G. Volosniev, *Communications Physics* **3**, 10.1038/s42005-020-00445-8 (2020).
- [24] X. Yang, C. H. van der Wal, and B. J. van Wees, *Nano Letters* **20**, 6148 (2020).
- [25] A. G. Volosniev, H. Alpern, Y. Paltiel, O. Millo, M. Lemesko, and A. Ghazaryan, *Phys. Rev. B* **104**, 024430 (2021).
- [26] C. Kulkarni, A. K. Mondal, T. K. Das, G. Grinbom, F. Tassinari, M. F. J. Mabesoone, E. W. Meijer, and R. Naaman, *Advanced Materials* **32**, 1904965 (2020).
- [27] F. Evers, A. Aharony, N. Bar-Gill, O. Entin-Wohlman, P. Hedegård, O. Hod, P. Jelinek, G. Kamieniarz, M. Lemesko, K. Michaeli, V. Mujica, R. Naaman, Y. Paltiel, S. Refaely-Abramson, O. Tal, J. Thijssen, M. Thoss, J. M. van Ruitenbeek, L. Venkataraman, D. H. Waldeck, B. Yan, and L. Kronik, *Advanced Materials* **34**, 2106629 (2022).
- [28] S. F. Ozturk, Z. Liu, J. D. Sutherland, and D. D. Sasselov, *Science Advances* **9**, 10.1126/sciadv.adg8274 (2023).
- [29] M. R. Wasielewski, *Physics Today* **76**, 28 (2023).
- [30] C. M. Niman, N. Sukenik, T. Dang, J. Nwachukwu, M. A. Thirumurthy, A. K. Jones, R. Naaman, K. Santra, T. K. Das, Y. Paltiel, L. T. Baczewski, and M. Y. El-Naggar, *The Journal of Chemical Physics* **159**, 145101 (2023).
- [31] G. Menichetti, L. Cavicchi, L. Lucchesi, F. Taddei, G. Iannaccone, P. Jarillo-Herrero, C. Felser, F. H. Koppen, and M. Polini, *Newton* **1**, 100013 (2025).
- [32] Y. Kapon, F. Kammerbauer, T. Balland, S. Yochelis, M. Kläui, and Y. Paltiel, *Nano Letters* **25**, 306 (2025).
- [33] A. Moharana, Y. Kapon, F. Kammerbauer, D. Anthofer, S. Yochelis, H. Shema, E. Gross, M. Kläui, Y. Paltiel, and A. Wittmann, *Science Advances* **11**, 10.1126/sciadv.ado4285 (2025).
- [34] J. Fransson, *The Journal of Physical Chemistry Letters* **10**, 7126–7132 (2019).
- [35] A. Ghazaryan, Y. Paltiel, and M. Lemesko, *The Journal of Physical Chemistry C* **124**, 11716 (2020).
- [36] P. Hedegård, *The Journal of Chemical Physics* **159**, 10.1063/5.0160233 (2023).
- [37] R. Alhyder, A. Cappellaro, M. Lemesko, and A. G. Volosniev, *The Journal of Chemical Physics* **159**, 104103 (2023).
- [38] R. Alhyder, M. Lemesko, and A. Cappellaro, *The Journal of Chemical Physics* **162**, 234106 (2025).
- [39] M. Di Ventura, R. Gutierrez, and G. Cuniberti, *The Journal of Physical Chemistry A* **129**, 9504–9510 (2025).
- [40] B. D. Josephson, *Physics Letters* **1**, 251 (1962).
- [41] A. F. Andreev, *Soviet Physics JETP* **19**, 1823 (1964).
- [42] G. E. Blonder, M. Tinkham, and T. M. Klapwijk, *Phys. Rev. B* **25**, 4515 (1982).
- [43] C. W. J. Beenakker and H. van Houten, *Phys. Rev. Lett.* **66**, 3056 (1991).
- [44] A. A. Golubov, M. Y. Kupriyanov, and E. Il'ichev, *Rev. Mod. Phys.* **76**, 411 (2004).
- [45] J. Clarke and F. K. Wilhelm, *Nature* **453**, 1031 (2008).
- [46] M. H. Devoret and R. J. Schoelkopf, *Science* **339**, 1169 (2013).
- [47] G. Wendin, *Reports on Progress in Physics* **80**, 106001 (2017).
- [48] M. Kjaergaard, M. E. Schwartz, J. Braumüller, P. Krantz, J. I.-J. Wang, S. Gustavsson, and W. D. Oliver, *Annual Review of Condensed Matter Physics* **11**, 369 (2020).
- [49] P. Krantz, M. Kjaergaard, F. Yan, T. P. Orlando, S. Gustavsson, and W. D. Oliver, *Applied Physics Reviews* **6**, 021318 (2019).
- [50] Y. A. Bychkov and É. I. Rashba, *Soviet Journal of Experimental and Theoretical Physics Letters* **39**, 78 (1984).
- [51] A. Manchon, H. C. Koo, J. Nitta, S. M. Frolov, and R. A. Duine, *Nature Materials* **14**, 871 (2015).
- [52] D. Bercioux and P. Lucignano, *Reports on Progress in Physics* **78**, 106001 (2015).
- [53] A. Buzdin, *Phys. Rev. Lett.* **101**, 107005 (2008).
- [54] P. T. Orban, G. Bassen, E. N. Crites, T. Matsuo, M. A. Siegler, and T. M. McQueen, *Communications Physics*

- [10.1038/s42005-026-02564-0](https://doi.org/10.1038/s42005-026-02564-0) (2026).
- [55] H. Alpern, K. Yavilberg, T. Dvir, N. Sukenik, M. Klang, S. Yochelis, H. Cohen, E. Grosfeld, H. Steinberg, Y. Paltiel, and O. Millo, *Nano Letters* **19**, 5167–5175 (2019).
- [56] C. W. Groth, M. Wimmer, A. R. Akhmerov, and X. Waintal, *New Journal of Physics* **16**, 063065 (2014).
- [57] T. Kloss, J. Weston, B. Gaury, B. Rossignol, C. Groth, and X. Waintal, *New Journal of Physics* **23**, 023025 (2021).
- [58] W. Yi, S. Wei, and Z. Guang-Hui, *Chin. Phys. Lett.* **23**, 3065 (2006).
- [59] Q.-f. Sun, X. C. Xie, and J. Wang, *Physical Review Letters* **98**, 196801 (2007).